

Effect of organic cations in locally concentrated ionic liquid electrolytes on the electrochemical performance of lithium metal batteries

Original

Effect of organic cations in locally concentrated ionic liquid electrolytes on the electrochemical performance of lithium metal batteries / Liu, X.; Mariani, A.; Zarrabeitia, M.; Di Pietro, M. E.; Dong, X.; Elia, G. A.; Mele, A.; Passerini, S.. - In: ENERGY STORAGE MATERIALS. - ISSN 2405-8297. - ELETTRONICO. - 44:(2022), pp. 370-378. [10.1016/j.ensm.2021.10.034]

Availability:

This version is available at: 11583/2958992 since: 2022-03-24T10:14:11Z

Publisher:

Elsevier B.V.

Published

DOI:10.1016/j.ensm.2021.10.034

Terms of use:

This article is made available under terms and conditions as specified in the corresponding bibliographic description in the repository

Publisher copyright

Elsevier postprint/Author's Accepted Manuscript

© 2022. This manuscript version is made available under the CC-BY-NC-ND 4.0 license
<http://creativecommons.org/licenses/by-nc-nd/4.0/>. The final authenticated version is available online at:
<http://dx.doi.org/10.1016/j.ensm.2021.10.034>

(Article begins on next page)

Effect of organic cations in locally concentrated ionic liquid electrolytes on the electrochemical performance of lithium metal batteries

Abstract

Organic cations are essential components of locally concentrated ionic liquid electrolytes (LCILEs), but receive little attention. Herein, we demonstrate their significant influence on the electrochemical performance of lithium metal batteries via a comparison study of two LCILEs employing either 1-butyl-1-methylpyrrolidinium cation (Pyr_{14}^+) or 1-ethyl-3-methylimidazolium cation (Emim^+). It is demonstrated that the structure of the organic cation in LCILEs has only a limited effect on the Li^+ -bis(fluorosulfonyl)imide anion (FSI^-) coordination. Nonetheless, the coordination of FSI^- with the organic cations is different. The less coordination of FSI^- to Emim^+ than to Pyr_{14}^+ results in the lower viscosity and faster Li^+ transport in the Emim^+ based electrolyte (EmiBE) than the Pyr_{14}^+ -based electrolyte (PyrBE). Additionally, the chemical composition of the solid-electrolyte interphase (SEI) formed on lithium metal is affected by the organic cations. A more stable SEI growing in the presence of Emim^+ leads to a higher lithium plating/stripping Coulombic efficiency (99.2%). As a result, Li/EmiBE/ $\text{LiNi}_{0.8}\text{Mn}_{0.1}\text{Co}_{0.1}\text{O}_2$ cells exhibit a capacity of 185 mAh g^{-1} at 1C discharge (2 mA cm^{-2}) and capacity retention of 96% after 200 cycles. Under the same conditions, PyrBE-based cells show only 34 mAh g^{-1} capacity with 39.6% retention.

Keywords: organic cations, ionic liquids, locally concentrated electrolytes, lithium metal batteries

1. Introduction

Lithium metal, with its high theoretical specific capacity (3860 mAh g⁻¹) and low redox potential (-3.04 V vs. SHE), is the ideal anode material for the next-generation high-energy-density rechargeable batteries, i.e., lithium metal batteries (LMBs) [1]. Nonetheless, lithium dendrite formation, limited plating/stripping Coulombic efficiency (CE), and safety concern are still blocking the road to room-temperature LMBs' application [2,3]. Among the strategies proposed to mitigate these issues [4–6], electrolyte design via selecting and adjusting electrolyte components, e.g., lithium salt and solvent, appears to be one of the most effective and feasible approaches [7–10].

Ionic liquids (ILs), exhibiting low flammability and high compatibility with lithium metal anodes, are promising electrolyte candidates for long-life and safe LMBs [11]. But their sluggish Li⁺ transport at room temperature limits the rate capability of the cell [12,13]. Recently, adding non-solvating and low-viscosity hydrofluoroether (HFE) to IL-based electrolytes has been proven an effective strategy in promoting the Li⁺ transport without compromising the Li plating/stripping CE, thanks to the reduced solution viscosity and unlocked hopping-type Li⁺ transport [14–16]. Such HFE-ILs hybrid electrolytes are named as locally concentrated ionic liquid electrolytes (LCILEs) [14–16]. Despite substantial improvement with respect to bare IL electrolytes, the cells employing the LCILEs with optimized Li⁺ concentration, anion and HFE, still exhibit limited rate capability when the current density approaches 2 mA cm⁻² [14,16]. Therefore, further rational design of the components is still required to break this limitation.

Organic cations are also essential components of LCILEs. Begić et al. demonstrated that the organic cation affects the electrical double layer at the electrode/IL electrolyte interface employing atomic force microscopy and molecular dynamics (MD) simulations [17,18]. Based on X-ray photoelectron spectroscopy (XPS) and mass spectrometry investigations, it has been recently proposed that organic cation also participates in the formation of solid-electrolyte interphase (SEI) in IL electrolytes [13,19,20]. The interfacial properties, including the electrical double layer and SEI, are crucial for the electrochemical performance of the lithium metal anode (LMA) [21–26]. Therefore, further optimization of the organic cation of LCILEs may promote Li^+ transport and cell performance. Nonetheless, the organic cation receives little attention in the investigation of LCILEs. Their role in the electrolytes' ion-coordination and SEI formation remains unclear.

The most commonly used organic cations in LCILEs are pyrrolidinium cations [14,16], e.g., 1-butyl-1-methylpyrrolidinium cation (Pyr_{14}^+ , $\text{C}_9\text{H}_{20}\text{N}^+$). 1-ethyl-3-methylimidazolium cation (Emim^+ , $\text{C}_6\text{H}_{11}\text{N}_2^+$), exhibiting rather different conformation, could lead to different ion-ion interaction. It has been reported that Emim^+ -based IL electrolytes offer lower solution viscosity and, consequently, faster Li^+ -ion transport than Pyr_{14}^+ -based IL electrolytes [27,28]. Moreover, the different chemical composition of Emim^+ and Pyr_{14}^+ may result in different SEI chemistries. To the best of our knowledge, Emim^+ -based LCILEs have not been studied yet.

Herein, the physicochemical characteristics and the electrochemical performance in LMBs of two LCILEs, i.e., $[\text{LiFSI}]_1[\text{EmimFSI}]_2[\text{BTfE}]_2$ (EmiBE) and

[LiFSI]₁[Pyr₁₄FSI]₂[BTFE]₂ (PyrBE) (BTFE stands for bis(2,2,2-trifluoroethyl) ether (a typical HFE solvent) and FSI is the bis(fluorosulfonyl) imide anion), are investigated to understand the influence of the organic cations. The chemical sketches of the components are shown in **Figure S1**. Compared with PyrBE, EmiBE exhibits faster Li⁺ transport and higher lithium plating/stripping Coulombic efficiency (99.2%). As a result, Li/EmiBE/LiNi_{0.8}Mn_{0.1}Co_{0.1}O₂ cells exhibit superior rate capability and cyclability with respect to PyrBE-based cells. Besides, investigations of the ion-ion interaction, solution structure, and solid-electrolyte interphase's chemical composition were also carried out to elucidate the role of the organic cation.

2. Material and methods

2.1. Materials

Molecular sieves (3 Å, Alfa Aesar) were activated at 300 °C under vacuum (10⁻³ mbar) for more than one week. BTFE (98%, Sigma Aldrich) and DMC (Battery grade, UBE) were dried with the activated molecular sieves for three days before use. LiFSI (99%, PROVISCO CS) was dried at 120 °C under vacuum (10⁻³ mbar) for 24 h before use. EmimFSI (99.5%, Solvionic) and Pyr₁₄FSI (99.5%, solvionic) were dried stepwise from room temperature to 60 °C in vacuum range of 10⁻⁷ mbar for 3 days. Lithium metal foil (thickness 500 µm, Honji Metal Co., LTD) was used as received. PE sheet (SV718, Asahi Kasei Company) was dried at 40 °C under vacuum (10⁻³ mbar) for 24 h.

2.2. Electrolyte preparation and electrochemical measurements

The electrolyte preparation was carried out in an Ar-filled glove box with H₂O and O₂ levels < 0.1 ppm. The dried LiFSI was firstly dissolved in the dried EmimFSI or

Pyr₁₄FSI, and these binary electrolytes were further dried at 60 °C in vacuum range of 10⁻⁷ mbar for 3 days. The EmiBE and PyrBE ternary electrolytes were prepared via mixing the fully dried binary electrolytes with the pre-dried BTFE.

The NMC811 electrode tape with Al as current collector were purchased from Targray, consisting 90 wt. % NMC811, 5 wt % PVDF binder, and 5 wt % Super P. The mass loading of NMC811 is 10 mg cm⁻². The cathode tap was cut into disks with a diameter of 1.2 cm and then dried at 110 °C under vacuum (10⁻³ mbar) for 12 h before use.

CR2032-type coin cells employing lithium discs with a diameter of 14 mm as counter electrode and the dried PE discs as separators were assembled. 75 µL electrolytes were added to each cell. For Li/Li, Li/Cu, and Li/NMC811 cells, lithium discs (Φ = 14 mm), Cu foil (Φ = 19 mm), and NMC811 electrode (Φ = 12 mm) were used as the working electrodes, respectively. All the electrochemical measurements were carried out at 20 °C. The galvanostatic measurements were performed with a Maccor series 4000 battery cycler. The impedance evolution of the Li/Li coin cells employing different electrolytes upon cycling was measured with the VMP in the frequency range of 1 MHz to 50 mHz with a sinusoidal perturbation of 10 mV.

2.3. Characterization

The self-diffusion coefficient of the species in the electrolytes were examined via pulsed field gradient (PFG) NMR. The samples were prepared in a dry room with a dew point < -70°C. The EmiBE and PyrBE ternary electrolytes were transferred to 5 mm NMR tubes, equipped with a capillary containing deuterated dimethylsulfoxide

(DMSO- d_6), and immediately flame-sealed. NMR measurements were performed at 293 K without sample spinning with a Bruker NEO 500 console (11.74 T) equipped with a direct observe BBFO (broadband including fluorine) iProbe and a variable-temperature unit. The instrument was carefully tuned, shimmed, and the 90° pulses calibrated. ^1H , ^{19}F and ^7Li self-diffusion experiments were performed using the bipolar pulse longitudinal eddy current delay (BPP-LED) pulse sequence by applying sine-shaped pulsed magnetic field gradients along the z-direction up to a maximum strength of $G = 53.5 \text{ G cm}^{-1}$. Flash points of the electrolytes were measured using a Grabner Instruments MINIFLASH FLP flashpoint tester according to ASTM D6450-CCCFP (Flash-Point by Continuously Closed Cup) in the temperature range of 25-300 °C. The conductivity of the electrolytes was determined via electrochemical impedance spectroscopy by an integrated liquid conductivity system MCS 10 (Material Mates-Biologic) sealed high temperature conductivity cells (HTCC, Material Mates) with Pt-black electrodes were used. The conductivity values averaged over 60 min (around 60 data points) were used. The cell constants were determined using a 0.01 M KCl standard solution. The electrolytes' viscosity was tested in a dry room environment utilizing an Anton-Paar MCR 102 rheometer, applying a constant shear rate of 10 s^{-1} , and using a Peltier system for cooling/heating. The viscosity values averaged over 2.5 min (50 data points) are used. The Raman measurements were recorded on a RAM II FT-Raman module of a Bruker Vertex70v FT-IR spectrometer with a laser wavelength of 1064 nm and laser power of 300 mW. Scanning electronic microscopy (SEM) images were obtained using a Zeiss LEO 1550 microscope. The cross-section of the lithium

electrodes was made with a scissor in the glove box. XPS measurements were conducted in an ultrahigh vacuum surface analysis system (10^{-10} mbar) by Phoibos 150 XPS spectrometer (SPECS –Surface concept) equipped with a micro-channel plate and Delay Line Detector and monochromatized Al K_{α} (1486.6 eV) X-ray in a fixed analyzer transmission mode. The scans were acquired with an X-ray sources of 200 W, 30 eV pass energy and 0.1 eV energy step. The depth profiling was carried out using a focused ion gun for 5 keV Ar^{+} for 12 min, which correspond to an etching depth of 9.6 nm. Since polyhydrocarbons are expected on the surface of the deposited lithium metal due to the electrolyte decomposition, the photoelectron spectra were calibrated using C-C/C-H peak of polyhydrocarbons (285.0 eV) as reference [29,30]. The peak fitting was carried out by CasaXPS software, using Shiley-type background and 70% Gaussian – 30% Lorentzian profile function. For the post-mortem characterization, the electrodes were removed from cells and washed with the dried DMC in the Ar-filled glove box. The samples were sealed in transfer boxes to prevent exposure to humid air for SEM, and XPS measurements.

2.4. MD simulation

Molecular dynamics simulations were carried out using Amber 18 software [31] exploiting the GAFF force field [32]. The atomic partial charges were obtained with the RESP algorithm from DFT calculations run with Gaussian09e at the B3LYP/6-311++G** level of theory [33]. The starting random molecular arrangements were obtained by Packmol [34]. The simulation went through different steps starting from a geometrical relaxation, followed by a gradual heating of the system from 0 to 50K in

several NVT sessions. The systems were then equilibrated at 300K for 20ns in NPT ensemble, and for further 20ns in NVT. A final productive NVT phase of 10ns was then used for the analysis. For the productive phase the timestep used was 2fs, and the simulation was dumped every 1000 steps, obtaining a final trajectory of 5000 frames spaced by 2ps each. In order to account for charge transfer and polarization effects, the atomic charges of the ionic species were scaled by a factor 0.74, which is known to return reliable results for ionic liquids [35]. The trajectories were analyzed with Travis [36,37]. The simulation goodness was checked by comparing the theoretical and experimental densities as shown in the Table S1.

3. Results and Discussion

The formulation, density, and Li^+ concentration of the EmiBE and PyrBE are shown in **Table 1**. Due to the low weight content of the BTFE, i.e., 32.1% in EmiBE and 30.4% in PyrBE, no flash point is detected in the temperature range of 25-300 °C, indicating a low flammability of the electrolytes.

The ionic conductivities and viscosities of EmiBE and PyrBE at 20 °C are summarized in **Figure 1a** and **b**, respectively. As expected, EmiBE shows lower viscosity and higher ionic conductivity than PyrBE. The ionic conductivity of EmiBE is 9.6 mS cm^{-1} , which is higher than PyrBE (4.0 mS cm^{-1}) and the previously reported PyrBE-based LCILEs ($< 4 \text{ mS cm}^{-1}$) [14–16], demonstrating a superior ionic transport. It should be noticed that Li^+ , FSI⁻, and the organic cations all are ionic charge carriers and contribute to the ionic conductivity, while only Li^+ ions account for the operation of LMBs. Therefore, the self-diffusion coefficient (D_i) of the ions in the electrolytes

was examined via PFG-NMR. The results are shown in **Figure 1c**. All ionic species exhibit higher self-diffusion coefficients in EmiBE than PyrBE, well matching the lower viscosity of the former electrolyte. Specifically, the Li^+ self-diffusion coefficient in PyrBE is $1.92 \times 10^{-11} \text{ m}^2 \text{ s}^{-1}$, which is close to the value reported for Pyr_{13}^+ -based LCILE [14]. In comparison, EmiBE exhibits a higher Li^+ diffusion coefficient, $3.50 \times 10^{-11} \text{ m}^2 \text{ s}^{-1}$, indicating for a higher mobility of Li^+ .

The apparent Li^+ transference numbers are calculated according to the following equation:

$$t = \frac{D_{\text{Li}}x_{\text{Li}}}{D_{\text{Li}}x_{\text{Li}} + D_{\text{FSI}}x_{\text{FSI}} + D_{\text{Emim/Pyr14}}x_{\text{Emim/Pyr14}}}$$

where x_i denotes the mole fraction of the ionic species i . For example, the x_{Li} , x_{FSI} , and x_{Emim} of EmiBE is 1/6, 2/6, and 3/6, respectively. The calculated apparent Li^+ transference numbers in EmiBE and PyrBE are 0.12 and 0.13, respectively. Considering the higher ionic conductivity of EmiBE than PyrBE and the similar apparent Li^+ transference number in these two electrolytes, one can infer that EmiBE exhibits a faster Li^+ transport than PyrBE, which is identical to the higher Li^+ self-diffusion coefficient in EmiBE. The superior Li^+ transport in EmiBE is beneficial to cells' rate capability.

The physicochemical properties are usually associated with the microstructure of the solution, e.g., ion-ion interactions [38–40]. However, the Raman spectra (as shown in **Figure S2**) reveal similar Li^+ -FSI $^-$ coordination in EmiBE and PyrBE. The average number of FSI $^-$ coordinating to each Li^+ is 2.66 and 2.72 in EmiBE and PyrBE, respectively. Therefore, the organic cation has a minimal effect on the Li^+ -FSI $^-$

coordination. Due to the intrinsic difference between the organic cations, i.e., Emim⁺ and Pyr₁₄⁺, their coordination difference is not accessible via Raman spectroscopy.

To understand the difference in the solution structure of the two electrolytes, MD simulations were performed. The computed densities of EmiBE (1.5297 g cm⁻³) and PyrBE (1.4487 g cm⁻³) from MD simulations match well with the experimental data, respectively, 1.5334 g cm⁻³ and 1.4369 g cm⁻³, indicating for the quality of the simulations. The snapshots of EmiBE and PyrBE are displayed in **Figure 2a** and **b**, respectively. The yellow spheres, red sticks, blue sticks, and cyan clouds represent Li⁺, organic cation, FSI⁻, and BTFE, respectively. A microheterogeneity can be seen in both electrolyte solutions. Most ions, including Li⁺, FSI⁻, and organic cations, gather forming ionic networks. BTFE with a few FSI⁻ and organic cations, but no Li⁺, produces a micro-domain distinguished from the ionic network. Taking a close look at the ionic network, one can find that Li⁺ ions are directly coordinated by the FSI⁻ anions, which are further surrounded by the organic cations.

The solvation of Li⁺ with the oxygen atoms in FSI⁻ was first characterized by means of radial distribution functions (RDF) as shown in **Figure 2c**. RDF profiles of both systems show a sharp peak at 2.1 Å which indicates strong interaction between Li⁺ and FSI⁻. To further check for differences in the Li⁺-FSI⁻ interactions of the two systems, the Li⁺ coordination number population has been extracted, showing, again, not a big difference between the two systems. Both of them have a probability larger than 60% for a Li⁺ to be surrounded by five oxygen atoms; the average number of oxygen atoms from FSI⁻ coordinating to each Li⁺ was calculated to be 4.8 and 4.7 for EmiBE and

PyrBE, respectively. The similar Li^+ -FSI $^-$ coordination concluded from the MD simulation is identical to what has been observed from Raman spectra (**Figure S2**), further confirming the goodness of the MD model. Therefore, the differences between the electrolytes cannot originate from the Li^+ -FSI $^-$ solvation properties. It should be noted that five coordinating oxygen atoms do not mean five FSI $^-$ anions in the first solvation shell of Li^+ , as each FSI $^-$ has, potentially, four oxygen coordination sites.

The focus is then shifted to the organic cations, i.e., the only chemically different species in the two electrolyte systems. The geometric center of ring was taken as a reference to check the corresponding RDF with the oxygen atoms from FSI $^-$. The RDF patterns, shown in **Figure 2e**, appear to be markedly different. The analysis of the coordination number population evidences distinct results: Emim $^+$ is coordinated on average by 3.6 oxygen atoms from FSI $^-$, while Pyr $_{14}^+$ has on average 4.4 oxygen atoms from FSI $^-$ in its first solvation shell.

The coordination of BTFE has been also extracted, but is very similar in both electrolyte systems (**Figure S3**). Therefore, the most significant difference in these two electrolyte solutions is the coordination of the organic cations and FSI $^-$. Compared with that of Pyr $_{14}^+$, the less coordination of Emim $^+$ with FSI $^-$ is beneficial to a lower solution viscosity, contributing to the faster Li^+ transport in EmiBE [41].

The electrochemical performance of LMAs in the two electrolytes were evaluated in Li/Li and Li/Cu cells at 20 °C. **Figure 3a** shows the Li/Li cells' voltage profiles at different current densities, but a constant capacity of 1 mAh cm $^{-2}$ for each stripping/plating cycle. The cell employing EmiBE shows a polarization of 138 mV at

2 mA cm⁻², and can operate at a current as high as 3.0 mA cm⁻². When PyrBE is used as the electrolyte, much higher cell polarizations are observed, e.g., 252 mV at 2 mA cm⁻², and short circuit occurs already during the cycling at 2.5 mA cm⁻². The superior rate performance of the LMAs in EmiBE is associated with its faster Li⁺ transport with respect to PyrBE.

Despite the lower cathodic stability of Emim⁺ with respect to Pyr₁₄⁺, [42] the severe cathodic decomposition of EmiBE is not seen from the linear sweep voltammograms (LSVs) of Cu working electrodes (**Figure S4a**). Moreover, the replacement of Pyr₁₄⁺ with Emim⁺ even promotes the Li stripping/plating CE which was evaluated via the cycling of lithium metal deposited on Cu [43]. Before cycling, one formation cycle was performed plating 5 mAh cm⁻² of Li on the Cu substrate and stripping the Li to 1 V. Afterward, 5 mAh cm⁻² Li was first deposited on the Cu electrode to grant a Li reservoir, followed by repeatedly Li stripping/plating at 1 mAh cm⁻² for 11 cycles. Finally, the remaining Li metal after the 11 cycles was stripped to 1 V. The voltage evolution of the cells upon the measurement is shown in **Figure 3b**. By dividing the total stripping capacity by the total plating capacity after the initial formation cycle, the average CE is calculated to be 99.2% and 98.8% for EmiBE and PyrBE, respectively. The cyclability of LMA in these two electrolytes was further assessed in Li/Li symmetric cells via continuous galvanostatic cycling at a current density of 1.0 mA cm⁻² and a cycling capacity of 1 mAh cm⁻² (2 h/cycle). The voltage evolution is shown in **Figure 2c**. The cell employing PyrBE exhibits a rapid increase of cell polarization (from 128 mV at the 50th cycle to 254 mV at the 300th cycle) and a limited cyclability (332 cycles). In

contrast, the cell employing EmiBE exhibits a slower polarization increase (from 71 mV at the 50th cycle to 117 mV at the 300th cycle) and a cyclability exceeding 500 cycles. The voltage profiles of the cells during a few selected cycles are shown in **Figure S5**. The Nyquist plots of the Li/Li cells after different cycles (1-240 cycles) are shown in **Figure S6**. The ohmic and interfacial resistances increase upon cycling in PyrBE, revealing continuous degradation of electrolyte and LMA in PyrBE, but are quite stable in EmiBE, indicating for a higher stability of the Li/EmiBE interface [23,44].

The more severe degradation of LMA in PyrBE is clearly visualized by the SEM images of the lithium metal electrodes after 100 stripping/plating cycles (1 mA cm^{-2} , 1 mAh cm^{-2}). EmiBE leads a denser surface layer (**Figure 3d**), while the surface of the lithium electrode cycled in PyrBE is porous (**Figure 3e**). Remarkable difference is also seen from the cross-sectional SEM images of the cycled lithium foils. After cycling in EmiBE, the surface layer on top of the bulk lithium has a thickness of $28 \text{ }\mu\text{m}$ (**Figure 3f**), while, in high contrast, the one observed on the lithium metal cycled in PyrBE is $87 \text{ }\mu\text{m}$ (**Figure 3g**). SEM images with higher magnification can be found in **Figure S7**. This agrees with a more stable SEI on LMA in EmiBE.

To investigate the difference of the LMAs' surface chemistry in EmiBE and PyrBE, XPS analysis of Li metal deposited on a Cu substrate at 0.5 mA cm^{-2} for 3 h was performed. The morphology of the deposited Li is displayed in **Figure S7**.

Figure 4a shows the results obtained for the lithium metal deposited from EmiBE. From the surface survey, the presence of C=C (284.4 eV) [45], C-N (287.4 eV) [46],

and N-C=N (288.9 eV) [47,48] in the C 1s spectrum clearly results from the decomposition of Emim⁺, demonstrating that the organic cations do contribute to the SEI formation on deposited Li metal. The peak at 291.4 eV is assigned to C-F groups from the decomposition of BTFE [29]. The C-C/C-H peak at 285.0 eV originates from the decomposition of Emim⁺ and/or BTFE. In the O1s spectrum, two minor peaks at 530.5 eV and 531.4 eV are assigned to Li₂O and LiOH [45], respectively, while two dominant peaks at 533.3 eV and 534.9 eV reflect the O-S (SO_x) groups from FSI⁻ and the O-C group from BTFE [49], respectively. The presence of the decomposition products of BTFE (C-F at ~ 690 eV) and FSI⁻ (S-F at ~ 687 eV) is also seen in F 1s spectra. In N 1s spectra, four component peaks are identified. The smallest peak at 398.7 eV is assigned to Li₃N forming via the complete reduction of FSI⁻ [11]. The peak at 400.7 eV represents negatively charged nitrogen atoms (N⁻) from the FSI⁻ decomposition, while the peaks at 401.9 eV and 404.0 eV reflect the neutral (N⁰) and positively charged (N⁺) nitrogen atoms from the Emim⁺ decomposition, respectively [47,49]. As demonstrated in literature, the N⁺ of organic cations, e.g., Emim⁺ and Pyr₁₄⁺, can convert to N⁰ via C-N decomposition [50,51]. Therefore, the signal of N⁰ is relatively stronger than that of N⁺, although there is an equal amount of N⁺ and N⁰ in each Emim⁺ [19]. These results indicate that all the electrolyte components, i.e., Emim⁺, FSI⁻, and BTFE, contribute to the SEI formation on LMAs.

After 12 min Ar⁺ sputtering, the chemical composition of the SEI does not change, but small changes in the concentration of some species are observed. Deeper into the SEI, the signals of the species originating from the decomposition of Emim⁺ and BTFE,

e.g., C-N peak (C 1s), O-C peak (O 1s), and C-F peak (F 1s), show weakened intensities, indicating that these two species contribute more to the outermost SEI layer. In contrast, the features resulting from the FSI⁻ decomposition, e.g., O-S peak (O 1s), S-F peak (F 1s), N⁻ peak (N 1s), as well as Li₃N peak (N 1s), strengthen upon sputtering, suggesting an increased contribution of FSI⁻ to the deeper SEI layer.

The XPS results obtained with PyrBE are shown in **Figure 4b**. The signal of F 1s and N 1s show a much lower intensity than in EmiBE (note that the intensity scale is normalized). Especially for the N 1s spectrum, of which the signal-to-noise ratio is very low, leading to difficulties in the fitting. Compared with those in **Figure 4a**, the peaks representing the features of the FSI⁻ and BTFE decompositions, e.g., C-F peak (C 1s), O-S peak (O 1s), O-C peak (O 1s), C-F peak (F 1s), and S-F peak (F 1s), show much lower intensity, indicating a reduced contributions of these two species to the SEI. The Pyr₁₄⁺ decomposition is suggested by the presence of the C-N peak in the C 1s spectrum, but its intensity is much lower than that of the C-C/C-H peak, which is in strong contrast to what is observed for EmiBE (C 1s spectrum in **Figure 4a**). Such a difference can be explained by the different atomic ratio of C/N in Emim⁺ (3:1) and Pyr₁₄⁺ (9:1). The lower N content in Pyr₁₄⁺, together with the lower decomposition of FSI⁻, result in the relatively low intensity of the signals in the N 1s spectrum. The variation of the SEI chemical composition after the Ar⁺ sputtering shows a similar trend as the one formed in EmiBE. Even though more FSI⁻ and fewer Pyr₁₄⁺ decomposition species are evidenced, the overall trend described above does not substantially change.

Additionally, the PyrBE induced SEI is composed by another species related with carbon-oxygen bonds. As observed in **Figure 4b**, the peak at 288.6 eV in C 1s spectra and the peaks at 533.7 eV and 531.7 eV in O 1s spectra indicate the presence of O-C=O, which does not belong to the components of the Pyr₁₄⁺. The O-C=O group could be introduced by the decomposition of dimethyl carbonate used to wash the lithium electrode [52], which is not observed on the lithium electrode deposited from EmiBE. This is coherent with that the SEI formed in EmiBE to be more stable and protective than that in PyrBE, which well agrees with the electrochemical performance reported in **Figure 3**. The difference in the SEI formed on lithium metal in the two electrolytes clearly demonstrates the influence of the organic cations on the SEI' chemical composition and stability.

Due to a good anodic stability of the electrolytes (as shown in **Figure S4b**), Li/LiNi_{0.8}Mn_{0.1}Co_{0.1}O₂ (NMC811) coin cells were assembled and measured at 20 °C within the 2.8-4.4 V voltage window to further evaluate the influence of the ionic liquid cation. The mass loading of the NMC811 was 10 mg cm⁻², and the current collector is Al foils. Despite the use of the FSI⁻ anion, the electrolytes can still effectively passivate Al foil current collectors, avoiding severe anodic corrosion of Al current collectors as demonstrated in **Figure S8**.

The effects of discharge rates on the cell performance was first evaluated [53]. After five formation cycles at C/10 (1C = 2 mA cm⁻²), the cells were discharged at different C-rates with a constant charge rate of C/3. The discharge specific capacity upon the various measurements is summarized in **Figure 5a**. The specific capacity at

C/10 reaches 208 and 197 mAh g⁻¹ in EmiBE and PyrBE electrolytes, respectively. However, the cell employing PyrBE exhibits limited capacities of 181, 168, and 34 mAh g⁻¹ at the discharge rate C/3, C/2, and 1C, respectively. On the other hand, the cell using EmiBE delivers much higher capacities (198, 195, and 185 mAh g⁻¹ at C/3, C/2, and 1C, respectively). The dis-/charge profiles of the cells cycled at the different rates are shown in **Figure 5b** and **Figure S9**. The influence of the charge rate was also examined as summarized in **Figure S10**. For instance, with a charge rate of 1C and a discharge rate of C/3, the Li/EmiBE/NMC811 cell showed a high capacity of 191 mAh g⁻¹, while the Li/PyrBE/NMC811 cell cannot operate due to the lithium dendrite growth (**Figure S10d**). The significantly promoted rate capability obtained with EmiBE is clearly associated with the faster Li⁺ transport.

The cyclability of the Li/NMC811 cells was also evaluated with a charge rate of C/3 and a discharge rate of 1C after two formation cycles at C/10, as shown in **Figure 5c** [54]. PyrBE not only leads to a limited specific capacity but also to low capacity retention, 39.6%. In high contrast, the cell employing EmiBE exhibits a capacity retention of 96% after 200 cycles and an average CE of 99.91%, indicating superior cyclability and reversibility performance. The dis-/charge profiles of the cells at the selected cycled upon cycling are shown in **Figure S11**. After 200 cycles in EmiBE, the lithium metal anode only shows limited degradation (**Figure S12**), once again proving the high compatibility of EmiBE with LMAs.

4. Conclusions

The structure of the organic cation in LCILEs has only a limited effect on the Li^+ - FSI^- coordination. Nonetheless, the coordination of the organic cations to FSI^- is different, affecting the physical properties of the electrolyte solutions. The less coordination of FSI^- to Emim^+ than to Pyr_{14}^+ participates in a lower viscosity and a consequently faster Li^+ transport in EmiBE than PyrBE. Additionally, the two organic cations contribute differently to the SEI formation on lithium metal. In particular, the high N content of Emim^+ with respect to Pyr_{14}^+ results in a more stable SEI growing in the presence of the former cation. Overall, the use of Emim^+ organic cation is effective in optimizing the Li^+ ion transport and the chemistry and performance of the SEI formed on the Li anode, resulting in promoted electrochemical performance in terms of cyclability and rate capability of Li/Li and Li/NMC811 cells.

Appendices

Supporting Information is available from the internet or from the author.

References

- [1] J.G. Zhang, W. Xu, J. Xiao, X. Cao, J. Liu, Lithium Metal Anodes with Nonaqueous Electrolytes, *Chem. Rev.* 120 (2020) 13312–13348. <https://doi.org/10.1021/acs.chemrev.0c00275>.
- [2] G. Xu, L. Huang, C. Lu, X. Zhou, G. Cui, Revealing the multilevel thermal safety of lithium batteries, *Energy Storage Mater.* 31 (2020) 72–86. <https://doi.org/10.1016/j.ensm.2020.06.004>.
- [3] M. Li, C. Wang, Z. Chen, K. Xu, J. Lu, New Concepts in Electrolytes, *Chem. Rev.* 120 (2020) 6783–6819. <https://doi.org/10.1021/acs.chemrev.9b00531>.
- [4] W. Ye, L. Wang, Y. Yin, X. Fan, Y. Cheng, H. Gao, H. Zhang, Q. Zhang, G. Luo,

- M. Wang, Lithium Storage in Bowl-like Carbon: The Effect of Surface Curvature and Space Geometry on Li Metal Deposition, *ACS Energy Lett.* 6 (2021) 1811–1820. <https://doi.org/10.1021/acsenerylett.1c00456>.
- [5] T. Zhou, Y. Zhao, M. El Kazzi, J.W. Choi, A. Coskun, Stable Solid Electrolyte Interphase Formation Induced by Monoquat-Based Anchoring in Lithium Metal Batteries, *ACS Energy Lett.* 6 (2021) 1711–1718. <https://doi.org/10.1021/acsenerylett.1c00274>.
- [6] X.Q. Zhang, T. Li, B.Q. Li, R. Zhang, P. Shi, C. Yan, J.Q. Huang, Q. Zhang, A Sustainable Solid Electrolyte Interphase for High-Energy-Density Lithium Metal Batteries Under Practical Conditions, *Angew. Chemie - Int. Ed.* 59 (2020) 3252–3257. <https://doi.org/10.1002/anie.201911724>.
- [7] W. Deng, W. Dai, X. Zhou, Q. Han, W. Fang, N. Dong, B. He, Z. Liu, Competitive Solvation-Induced Concurrent Protection on the Anode and Cathode toward a 400 Wh kg⁻¹ Lithium Metal Battery, *ACS Energy Lett.* 6 (2021) 115–123. <https://doi.org/10.1021/acsenerylett.0c02351>.
- [8] X. Ren, L. Zou, S. Jiao, D. Mei, M.H. Engelhard, Q. Li, H. Lee, C. Niu, B.D. Adams, C. Wang, J. Liu, J.G. Zhang, W. Xu, High-concentration ether electrolytes for stable high-voltage lithium metal batteries, *ACS Energy Lett.* 4 (2019) 896–902. <https://doi.org/10.1021/acsenerylett.9b00381>.
- [9] S. Liu, X. Ji, N. Piao, J. Chen, N. Eidson, J. Xu, P. Wang, L. Chen, J. Zhang, T. Deng, S. Hou, T. Jin, H. Wan, J. Li, J. Tu, C. Wang, An Inorganic-Rich Solid Electrolyte Interphase for Advanced Lithium-Metal Batteries in Carbonate

- Electrolytes, *Angew. Chemie - Int. Ed.* 60 (2021) 3661–3671.
<https://doi.org/10.1002/anie.202012005>.
- [10] W. Xue, Z. Shi, M. Huang, S. Feng, C. Wang, F. Wang, J. Lopez, B. Qiao, G. Xu, W. Zhang, Y. Dong, R. Gao, Y. Shao-Horn, J.A. Johnson, J. Li, FSI-inspired solvent and “full fluorosulfonyl” electrolyte for 4 v class lithium-metal batteries, *Energy Environ. Sci.* 13 (2020) 212–220. <https://doi.org/10.1039/c9ee02538c>.
- [11] F. Wu, G.T. Kim, T. Diemant, M. Kuenzel, A.R. Schür, X. Gao, B. Qin, D. Alwast, Z. Jusys, R.J. Behm, D. Geiger, U. Kaiser, S. Passerini, Reducing Capacity and Voltage Decay of Co-Free $\text{Li}_{1.2}\text{Ni}_{0.2}\text{Mn}_{0.6}\text{O}_2$ as Positive Electrode Material for Lithium Batteries Employing an Ionic Liquid-Based Electrolyte, *Adv. Energy Mater.* 10 (2020) 2001830. <https://doi.org/10.1002/aenm.202001830>.
- [12] U. Pal, F. Chen, D. Gyabang, T. Pathirana, B. Roy, R. Kerr, D.R. MacFarlane, M. Armand, P.C. Howlett, M. Forsyth, Enhanced ion transport in an ether aided super concentrated ionic liquid electrolyte for long-life practical lithium metal battery applications, *J. Mater. Chem. A.* 8 (2020) 18826–18839. <https://doi.org/10.1039/d0ta06344d>.
- [13] K. Periyapperuma, E. Arca, S. Harvey, T. Pathirana, C. Ban, A. Burrell, C. Pozo-Gonzalo, P.C. Howlett, High Current Cycling in a Superconcentrated Ionic Liquid Electrolyte to Promote Uniform Li Morphology and a Uniform LiF-Rich Solid Electrolyte Interphase, *ACS Appl. Mater. Interfaces.* 12 (2020) 42236–42247. <https://doi.org/10.1021/acsami.0c09074>.
- [14] S. Lee, K. Park, B. Koo, C. Park, M. Jang, H. Lee, H. Lee, Safe, Stable Cycling

- of Lithium Metal Batteries with Low-Viscosity, Fire-Retardant Locally Concentrated Ionic Liquid Electrolytes, *Adv. Funct. Mater.* 30 (2020) 2003132. <https://doi.org/10.1002/adfm.202003132>.
- [15] Z. Wang, F. Zhang, Y. Sun, L. Zheng, Y. Shen, D. Fu, W. Li, A. Pan, L. Wang, J. Xu, J. Hu, X. Wu, Intrinsically Nonflammable Ionic Liquid-Based Localized Highly Concentrated Electrolytes Enable High-Performance Li-Metal Batteries, *Adv. Energy Mater.* 11 (2021) 2003752. <https://doi.org/10.1002/aenm.202003752>.
- [16] X. Liu, M. Zarrabeitia, A. Mariani, X. Gao, H.M. Schütz, S. Fang, T. Bizien, G.A. Elia, S. Passerini, Enhanced Li⁺ Transport in Ionic Liquid-Based Electrolytes Aided by Fluorinated Ethers for Highly Efficient Lithium Metal Batteries with Improved Rate Capability, *Small Methods*. (2021) 2100168. <https://doi.org/10.1002/smtd.202100168>.
- [17] S. Begić, H. Li, R. Atkin, A.F. Hollenkamp, P.C. Howlett, A comparative AFM study of the interfacial nanostructure in imidazolium or pyrrolidinium ionic liquid electrolytes for zinc electrochemical systems, *Phys. Chem. Chem. Phys.* 18 (2016) 29337–29347. <https://doi.org/10.1039/c6cp04299f>.
- [18] S. Begić, E. Jónsson, F. Chen, M. Forsyth, Molecular dynamics simulations of pyrrolidinium and imidazolium ionic liquids at graphene interfaces, *Phys. Chem. Chem. Phys.* 19 (2017) 30010–30020. <https://doi.org/10.1039/c7cp03389c>.
- [19] Y. Preibisch, F. Horsthemke, M. Winter, S. Nowak, A.S. Best, Is the Cation Innocent? An Analytical Approach on the Cationic Decomposition Behavior of

- N-Butyl- N-methylpyrrolidinium Bis(trifluoromethanesulfonyl)imide in Contact with Lithium Metal, *Chem. Mater.* 32 (2020) 2389–2398. <https://doi.org/10.1021/acs.chemmater.9b04827>.
- [20] K. Arano, S. Begic, F. Chen, D. Rakov, D. Mazouzi, N. Gautier, R. Kerr, B. Lestriez, J. Le Bideau, P.C. Howlett, D. Guyomard, M. Forsyth, N. Dupre, Tuning the Formation and Structure of the Silicon Electrode/Ionic Liquid Electrolyte Interphase in Superconcentrated Ionic Liquids, *ACS Appl. Mater. Interfaces*. 13 (2021) 28281–28294. <https://doi.org/10.1021/acsami.1c06465>.
- [21] X. Cao, P. Gao, X. Ren, L. Zou, M.H. Engelhard, B.E. Matthews, J. Hu, C. Niu, D. Liu, B.W. Arey, C. Wang, J. Xiao, J. Liu, W. Xu, J.G. Zhang, Effects of fluorinated solvents on electrolyte solvation structures and electrode/electrolyte interphases for lithium metal batteries, *Proc. Natl. Acad. Sci. U. S. A.* 118 (2021) e2020357118. <https://doi.org/10.1073/pnas.2020357118>.
- [22] N. Piao, X. Ji, H. Xu, X. Fan, L. Chen, S. Liu, M.N. Garaga, S.G. Greenbaum, L. Wang, C. Wang, X. He, Countersolvent Electrolytes for Lithium-Metal Batteries, *Adv. Energy Mater.* 10 (2020) 1903568. <https://doi.org/10.1002/aenm.201903568>.
- [23] L. Yu, S. Chen, H. Lee, L. Zhang, M.H. Engelhard, Q. Li, S. Jiao, J. Liu, W. Xu, J.G. Zhang, A Localized High-Concentration Electrolyte with Optimized Solvents and Lithium Difluoro(oxalate)borate Additive for Stable Lithium Metal Batteries, *ACS Energy Lett.* 3 (2018) 2059–2067. <https://doi.org/10.1021/acsenergylett.8b00935>.

- [24] C. Yan, Y.X. Yao, X. Chen, X.B. Cheng, X.Q. Zhang, J.Q. Huang, Q. Zhang, Lithium Nitrate Solvation Chemistry in Carbonate Electrolyte Sustains High-Voltage Lithium Metal Batteries, *Angew. Chemie - Int. Ed.* 57 (2018) 14055–14059. <https://doi.org/10.1002/anie.201807034>.
- [25] D.A. Rakov, F. Chen, S.A. Ferdousi, H. Li, T. Pathirana, A.N. Simonov, P.C. Howlett, R. Atkin, M. Forsyth, Engineering high-energy-density sodium battery anodes for improved cycling with superconcentrated ionic-liquid electrolytes, *Nat. Mater.* 19 (2020) 1096–1101. <https://doi.org/10.1038/s41563-020-0673-0>.
- [26] S.F. Ayatollahi, M. Bahrami, M.H. Ghatee, T. Ghaed-Sharaf, Simulating the Effect of Anions on Spreading of Nanodroplets and the Monolayer Behavior of Quaternary Ammonium-Based Ionic Liquids on Li(100) and Li(110) Metal Facets, *Ind. Eng. Chem. Res.* 59 (2020) 16258–16272. <https://doi.org/10.1021/acs.iecr.0c02442>.
- [27] H. Sun, G. Zhu, Y. Zhu, M.C. Lin, H. Chen, Y.Y. Li, W.H. Hung, B. Zhou, X. Wang, Y. Bai, M. Gu, C.L. Huang, H.C. Tai, X. Xu, M. Angell, J.J. Shyue, H. Dai, High-Safety and High-Energy-Density Lithium Metal Batteries in a Novel Ionic-Liquid Electrolyte, *Adv. Mater.* 32 (2020) 2001741. <https://doi.org/10.1002/adma.202001741>.
- [28] K. Matsumoto, E. Nishiwaki, T. Hosokawa, S. Tawa, T. Nohira, R. Hagiwara, Thermal, Physical, and Electrochemical Properties of Li[N(SO₂F)₂]-[1-Ethyl-3-methylimidazolium][N(SO₂F)₂] Ionic Liquid Electrolytes for Li Secondary Batteries Operated at Room and Intermediate Temperatures, *J. Phys. Chem. C.*

- 121 (2017) 9209–9219. <https://doi.org/10.1021/acs.jpcc.7b02296>.
- [29] J.J. Pireaux, High resolution XPS of organic polymers: the scienta ESCA300 database, *J. Electron Spectros. Relat. Phenomena.* 62 (1993) 371–372. [https://doi.org/10.1016/0368-2048\(93\)85006-7](https://doi.org/10.1016/0368-2048(93)85006-7).
- [30] R.I.R. Blyth, H. Buqa, F.P. Netzer, M.G. Ramsey, J.O. Besenhard, P. Golob, M. Winter, XPS studies of graphite electrode materials for lithium ion batteries, *Appl. Surf. Sci.* 167 (2000) 99–106. [https://doi.org/10.1016/S0169-4332\(00\)00525-0](https://doi.org/10.1016/S0169-4332(00)00525-0).
- [31] D.A. Case, T.E. Cheatham, T. Darden, H. Gohlke, R. Luo, K.M. Merz, A. Onufriev, C. Simmerling, B. Wang, R.J. Woods, The Amber biomolecular simulation programs, *J. Comput. Chem.* 26 (2005) 1668–1688. <https://doi.org/10.1002/jcc.20290>.
- [32] J. Wang, R.M. Wolf, J.W. Caldwell, P.A. Kollman, D.A. Case, Development and testing of a general Amber force field, *J. Comput. Chem.* 25 (2004) 1157–1174. <https://doi.org/10.1002/jcc.20035>.
- [33] M.J. Frisch, G.W. Trucks, H.B. Schlegel, G.E. Scuseria, M.A. Robb, J.R. Cheeseman, G. Scalmani, V. Barone, G.A. Petersson, H. Nakatsuji, X. Li, M. Caricato, A. Marenich, J. Bloino, B.G. Janesko, R. Gomperts, B. Mennucci, H.P. Hratchian, J. V. Ort, D.J. Fox, Gaussian 09, Revision D.01, (2009).
- [34] L. Martinez, R. Andrade, E.G. Birgin, J.M. Martínez, PACKMOL: A package for building initial configurations for molecular dynamics simulations, *J. Comput. Chem.* 30 (2009) 2157–2164. <https://doi.org/10.1002/jcc.21224>.

- [35] A. Mariani, R. Caminiti, M. Campetella, L. Gontrani, Pressure-induced mesoscopic disorder in protic ionic liquids: First computational study, *Phys. Chem. Chem. Phys.* 18 (2016) 2297–2302. <https://doi.org/10.1039/c5cp06800b>.
- [36] M. Brehm, B. Kirchner, TRAVIS - A free analyzer and visualizer for monte carlo and molecular dynamics trajectories, *J. Chem. Inf. Model.* 51 (2011) 2007–2023. <https://doi.org/10.1021/ci200217w>.
- [37] M. Brehm, M. Thomas, S. Gehrke, B. Kirchner, TRAVIS—A free analyzer for trajectories from molecular simulation, *J. Chem. Phys.* 152 (2020) 164105. <https://doi.org/10.1063/5.0005078>.
- [38] J. Fu, X. Ji, J. Chen, L. Chen, X. Fan, D. Mu, C. Wang, Lithium Nitrate Regulated Sulfone Electrolytes for Lithium Metal Batteries, *Angew. Chemie - Int. Ed.* 59 (2020) 22194–22201. <https://doi.org/10.1002/anie.202009575>.
- [39] R. Amine, J. Liu, I. Acznik, T. Sheng, K. Lota, H. Sun, C.J. Sun, K. Fic, X. Zuo, Y. Ren, D.A. EI-Hady, W. Alshitari, A.S. Al-Bogami, Z. Chen, K. Amine, G.L. Xu, Regulating the Hidden Solvation-Ion-Exchange in Concentrated Electrolytes for Stable and Safe Lithium Metal Batteries, *Adv. Energy Mater.* 10 (2020) 2000901. <https://doi.org/10.1002/aenm.202000901>.
- [40] Y. Yamada, J. Wang, S. Ko, E. Watanabe, A. Yamada, Advances and issues in developing salt-concentrated battery electrolytes, *Nat. Energy.* 4 (2019) 269–280. <https://doi.org/10.1038/s41560-019-0336-z>.
- [41] M. Kunze, S. Jeong, E. Paillard, M. Schönhoff, M. Winter, S. Passerini, New insights to self-aggregation in ionic liquid electrolytes for high-energy

- electrochemical devices, *Adv. Energy Mater.* 1 (2011) 274–281.
<https://doi.org/10.1002/aenm.201000052>.
- [42] G.B. Appetecchi, M. Montanino, M. Carewska, M. Moreno, F. Alessandrini, S. Passerini, Chemical-physical properties of bis(perfluoroalkylsulfonyl)imide-based ionic liquids, *Electrochim. Acta.* 56 (2011) 1300–1307.
<https://doi.org/10.1016/j.electacta.2010.10.023>.
- [43] B.D. Adams, J. Zheng, X. Ren, W. Xu, J.G. Zhang, Accurate Determination of Coulombic Efficiency for Lithium Metal Anodes and Lithium Metal Batteries, *Adv. Energy Mater.* 8 (2018) 1702097. <https://doi.org/10.1002/aenm.201702097>.
- [44] J.-J. Woo, V.A. Maroni, G. Liu, J.T. Vaughey, D.J. Gosztola, K. Amine, Z. Zhang, Symmetrical Impedance Study on Inactivation Induced Degradation of Lithium Electrodes for Batteries Beyond Lithium-Ion, *J. Electrochem. Soc.* 161 (2014) A827–A830. <https://doi.org/10.1149/2.089405jes>.
- [45] J.F. Moulder, W.F. Stickle, P.E. Sobol, K.D. Bomben, J.F. Moulder, W.F. Stickle, P.E. Sobol, K.D. Bomben, *Handbook of X-ray Photoelectron Spectroscopy*, Handb. X-Ray Photoelectron Spectrosc. (1995).
- [46] S. Bhattacharyya, C. Cardinaud, G. Turban, Spectroscopic determination of the structure of amorphous nitrogenated carbon films, *J. Appl. Phys.* 83 (1998) 4491–4500. <https://doi.org/10.1063/1.367211>.
- [47] K. Chen, Z. Chai, C. Li, L. Shi, M. Liu, Q. Xie, Y. Zhang, D. Xu, A. Manivannan, Z. Liu, Catalyst-Free Growth of Three-Dimensional Graphene Flakes and Graphene/g-C₃N₄ Composite for Hydrocarbon Oxidation, *ACS Nano.* 10 (2016)

- 3665–3673. <https://doi.org/10.1021/acsnano.6b00113>.
- [48] W.J. Ong, L.L. Tan, S.P. Chai, S.T. Yong, Graphene oxide as a structure-directing agent for the two-dimensional interface engineering of sandwich-like graphene-g-C₃N₄ hybrid nanostructures with enhanced visible-light photoreduction of CO₂ to methane, *Chem. Commun.* 51 (2015) 858–861. <https://doi.org/10.1039/c4cc08996k>.
- [49] H. Kim, F. Wu, J.T. Lee, N. Nitta, H.T. Lin, M. Oschatz, W. Il Cho, S. Kaskel, O. Borodin, G. Yushin, In situ formation of protective coatings on sulfur cathodes in lithium batteries with lifsi-based organic electrolytes, *Adv. Energy Mater.* 5 (2015) 1401792. <https://doi.org/10.1002/aenm.201401792>.
- [50] M.C. Kroon, W. Buijs, C.J. Peters, G.J. Witkamp, Decomposition of ionic liquids in electrochemical processing, *Green Chem.* 8 (2006) 241–245. <https://doi.org/10.1039/b512724f>.
- [51] J.B. Haskins, H. Yildirim, C.W. Bauschlicher, J.W. Lawson, Decomposition of Ionic Liquids at Lithium Interfaces. 2. Gas Phase Computations, *J. Phys. Chem. C.* 121 (2017) 28235–28248. <https://doi.org/10.1021/acs.jpcc.7b09658>.
- [52] A.M. Andersson, A. Henningson, H. Siegbahn, U. Jansson, K. Edström, Electrochemically lithiated graphite characterised by photoelectron spectroscopy, in: *J. Power Sources*, 2003: pp. 522–527. [https://doi.org/10.1016/S0378-7753\(03\)00277-5](https://doi.org/10.1016/S0378-7753(03)00277-5).
- [53] X. Cao, X. Ren, L. Zou, M.H. Engelhard, W. Huang, H. Wang, B.E. Matthews, H. Lee, C. Niu, B.W. Arey, Y. Cui, C. Wang, J. Xiao, J. Liu, W. Xu, J.G. Zhang,

- Monolithic solid–electrolyte interphases formed in fluorinated orthoformate-based electrolytes minimize Li depletion and pulverization, *Nat. Energy*. 4 (2019) 796–805. <https://doi.org/10.1038/s41560-019-0464-5>.
- [54] S. Jiao, J. Zheng, Q. Li, X. Li, M.H. Engelhard, R. Cao, J.G. Zhang, W. Xu, Behavior of Lithium Metal Anodes under Various Capacity Utilization and High Current Density in Lithium Metal Batteries, *Joule*. 2 (2018) 110–124. <https://doi.org/10.1016/j.joule.2017.10.007>.

Table 1. Compositions of the electrolytes

Electrolyte	Composition	Molar ratio	Mass ratio	Density (20 °C) / g cm⁻³	Li⁺ molarity (20 °C) / mol L⁻¹
EmiBE	LiFSI:EmimFSI:BTFE	1:2:2	0.165:0.514:0.321	1.5334	1.35
PyrBE	LiFSI:Pyr ₁₄ FSI:BTFE	1:2:2	0.156:0.539:0.304	1.4369	1.20

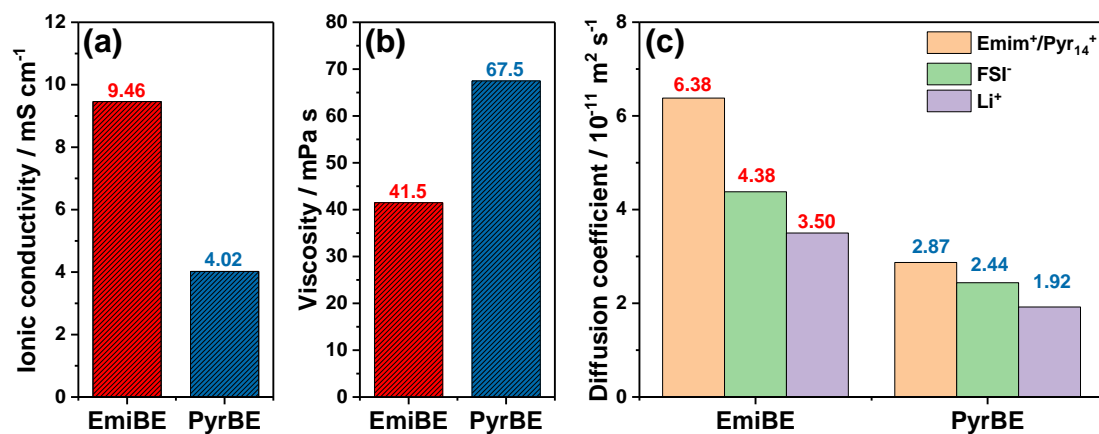


Figure 1. (a) Ionic conductivities and (b) viscosities of EmiBE and PyrBE at 20 °C. (c) Self-diffusion coefficients of ions in EmiBE and PyrBE measured via PFG-NMR at 20 °C.

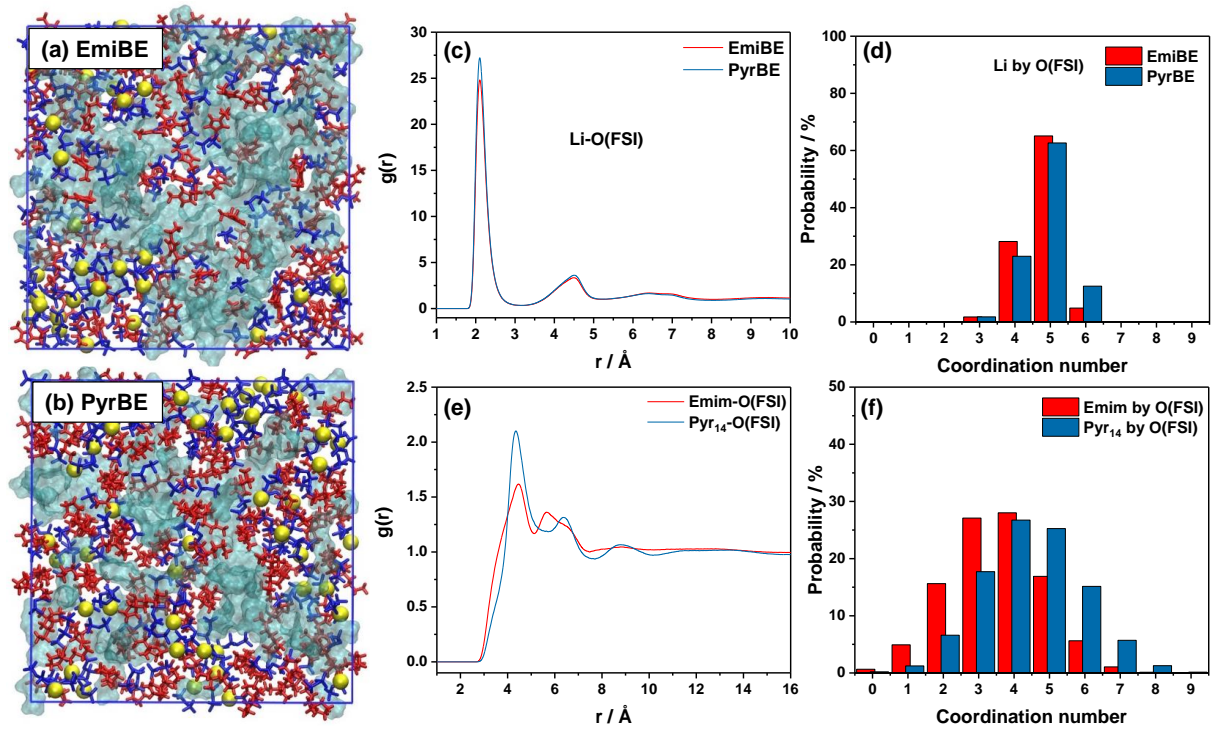


Figure 2. MD simulation for the EmiBE and PyrBE electrolytes. Snapshots of the MD simulated boxes for (a) EmiBE and (b) PyrBE electrolytes. The yellow spheres, red sticks, blue sticks, and cyan clouds represent Li^+ , organic cation, FSI^- , and BTFE, respectively. Radial distribution functions of (c) Li-O(FSI) and (e) $\text{Emim/Pyr}_{14}\text{-O(FSI)}$ pairs. Coordination number populations of (d) Li by O(FSI) , (e) $\text{Emim/Pyr}_{14} \text{ by O(FSI)}$.

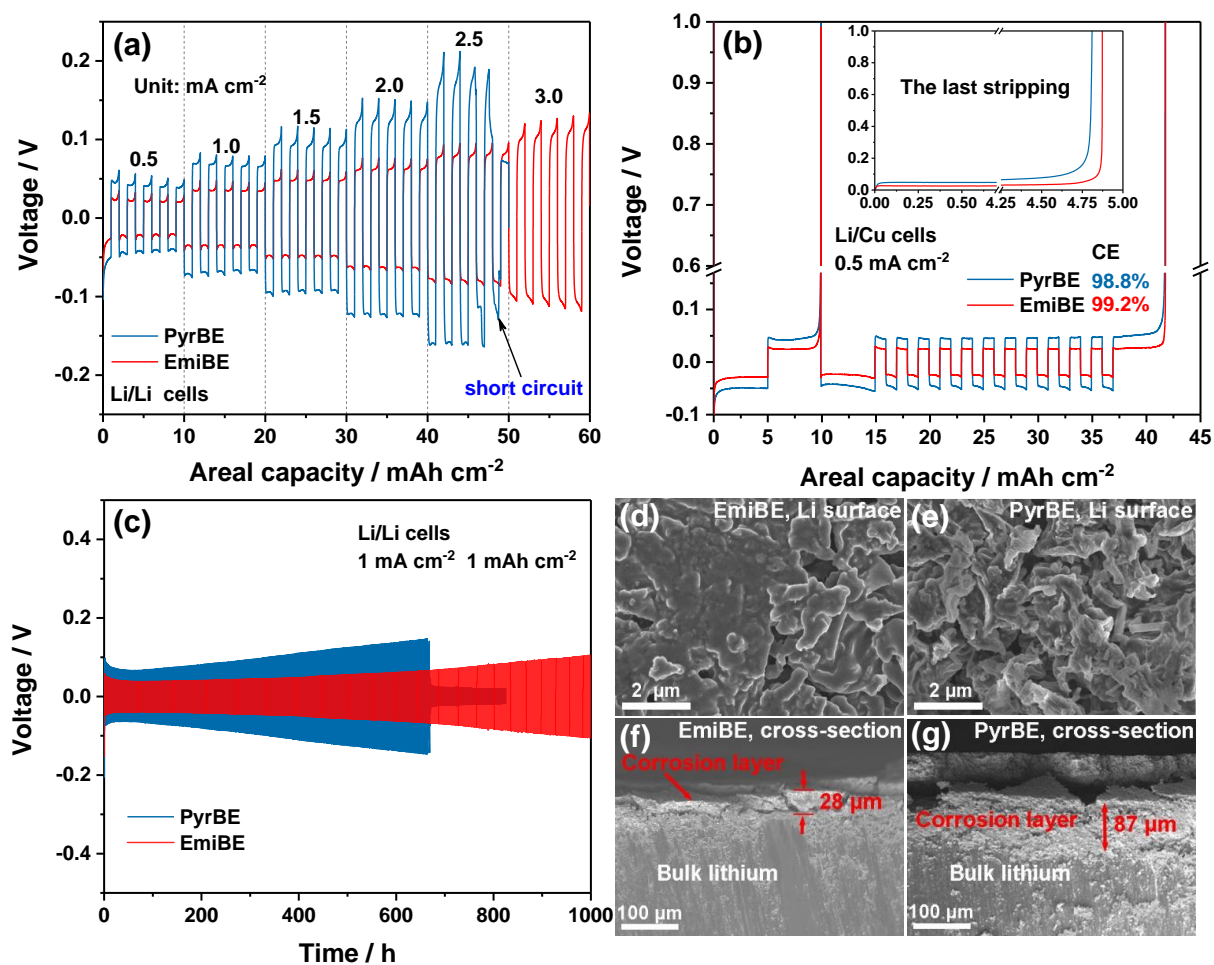


Figure 3. (a) Voltage profiles of Li plating/stripping processes in Li/Li cells at various current densities. (b) Li plating/stripping CE in Li/Cu cells. The inset shows the voltage profile of the last stripping process. (c) Long-term cycling voltage profiles for Li/Li cells. (d, e) Surface and (f, g) cross-section morphology of the Li foil after 100 cycles with a current density of 1 mA cm⁻² and a stripping-plating areal capacity of 1 mA cm⁻² in (d, f) EmiBE and (e, g) PyrBE electrolytes.

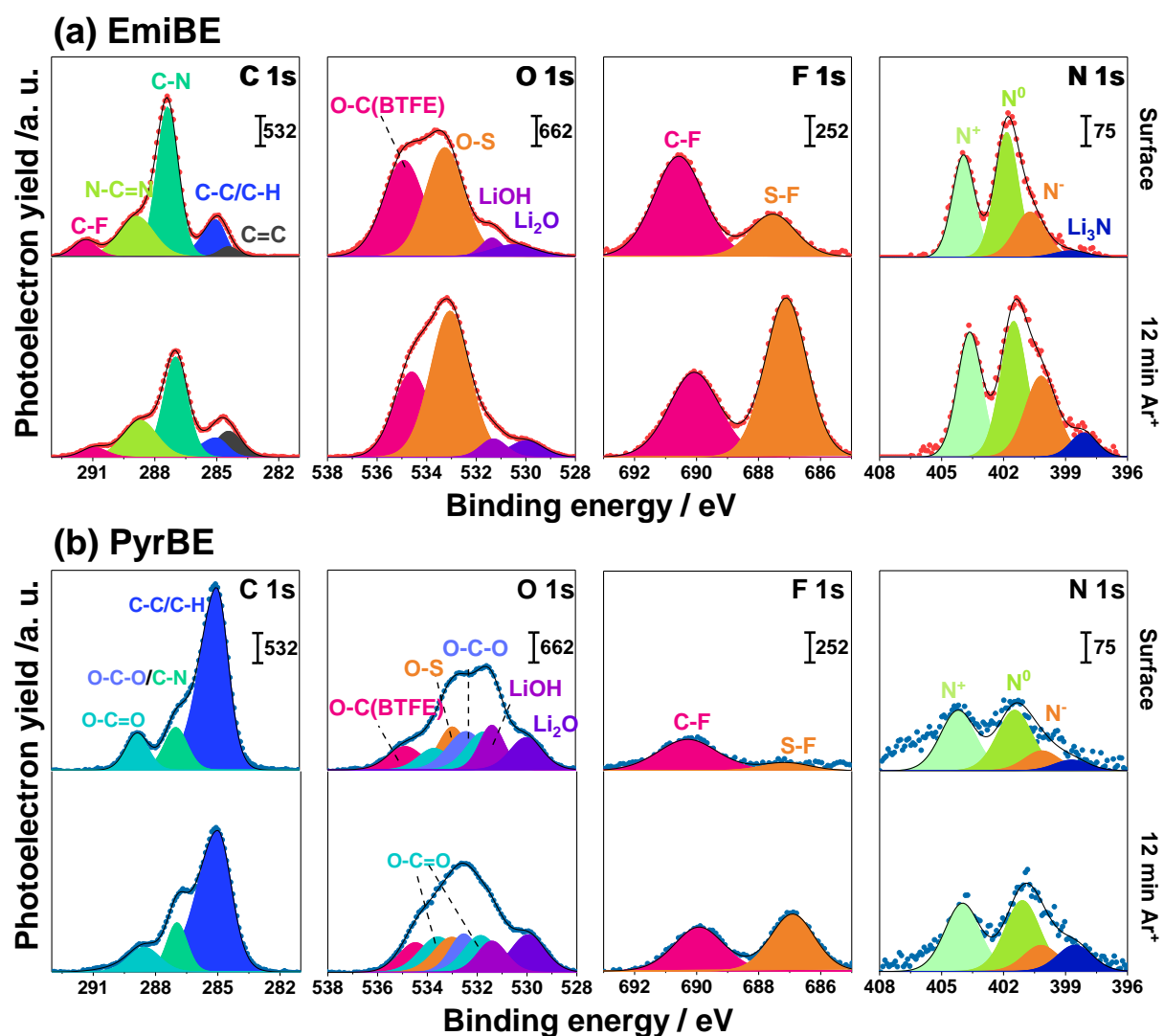


Figure 4. XPS analysis of C 1s, O 1s, F 1s, and N 1s photoelectron lines for the lithium (1.5 mAh cm^{-2}) deposited on Cu foil at 0.5 mA cm^{-2} in (a) EmiBE and (b) PyrBE electrolyte (surface and after Ar^+ sputtering for 12 min).

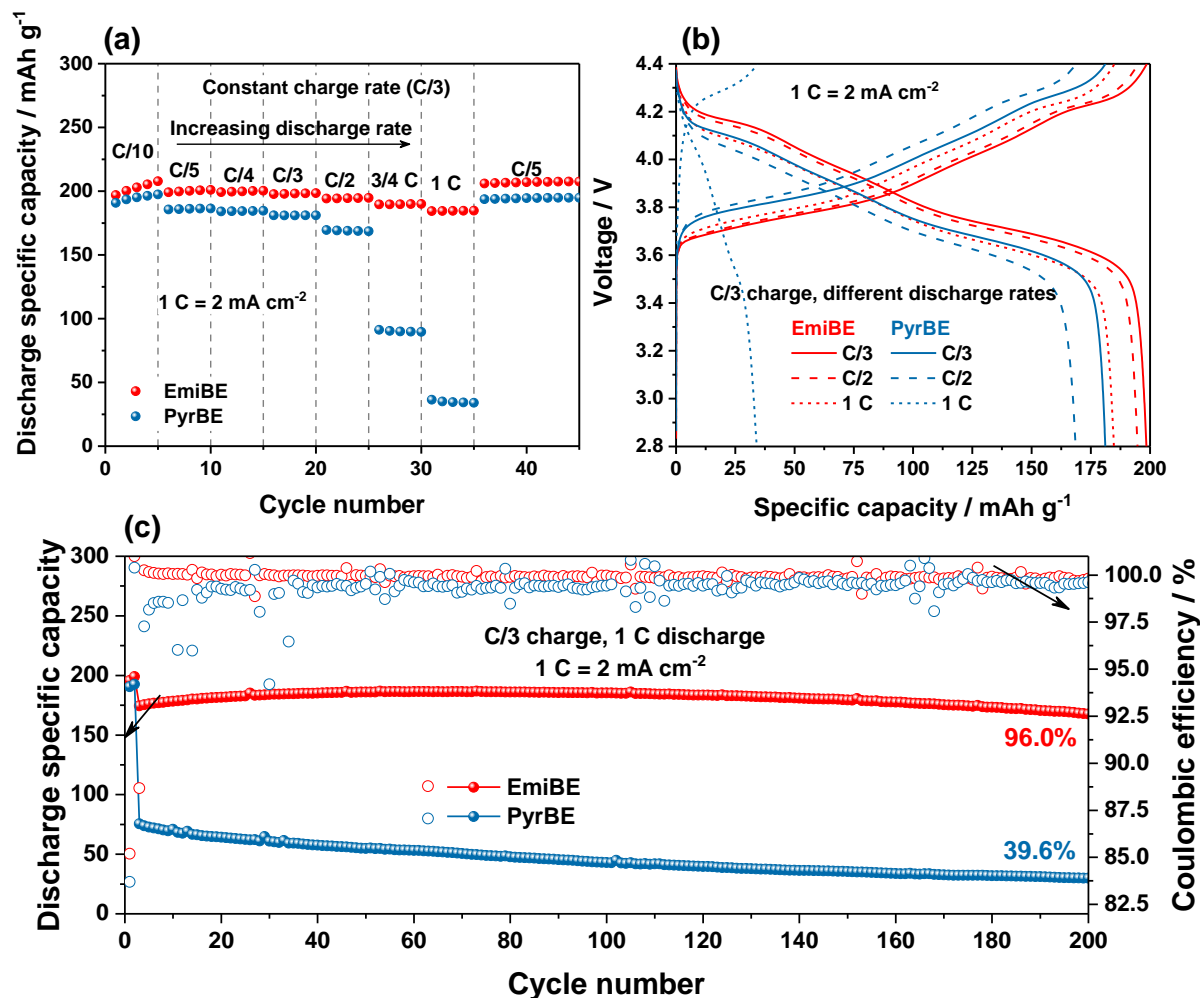


Figure 5. Performance of Li/NMC811 cells employing EmiBE and PyrBE electrolytes.

(a) Rate performance at different discharge C-rates with a constant charge rate of C/3 after five formation cycles at C/10. (b) The dis-/charge profiles of the cells at few selected C-rate. (c) The evolution of CE and discharge specific capacity upon long-term cycling of the cells with a charge rate of C/3 and a discharge rate of 1C after two formation cycles at C/10. The mass loading of NMC811 is 10 mg cm⁻². 1C is 200 mA g⁻¹, equaling to 2 mA cm⁻².